Research Article | Vol. 25, No. 4 | 20 Feb 2017 | OPTICS EXPRESS 3826

Optics EXPRESS

Integrated optical driver for interferometric optical gyroscopes

MINH A. TRAN,* TIN KOMLJENOVIC, JARED C. HULME, MJ KENNEDY, DANIEL J. BLUMENTHAL AND JOHN E. BOWERS

Department of Electrical and Computer Engineering, University of California, Santa Barbara, CA 93106, USA
**minhtran@ece.ucsb.edu*

Abstract: We present the first chip-scale "integrated optical driver" (IOD) that can interrogate with a sensing coil to realize an interferometric optical gyroscope. The chip comprises a light source, three photodiodes, two phase modulators and two 3-dB couplers within an area of 4.5 mm^2. This allows for a significant reduction in size, weight, power consumption and cost of optical gyroscopes.

OCIS codes: (280.4788) Optical sensing and sensors; (060.2800) Gyroscopes; (130.0130) Integrated optics.

References and links

1. A. Lawrence, *Modern Inertial Technology: Navigation, Guidance, and Control* (Springer, 1993).
2. H. C. Lefevre, *The Fiber-optic Gyroscope* (Artech house, 2014).
3. C. M. Smith, N. Venkataraman, M. T. Gallagher, D. Müller, J. A. West, N. F. Borrelli, D. C. Allan, and K. W. Koch, "Low-loss hollow-core silica/air photonic bandgap fibre," Nature **424**(6949), 657–659 (2003).
4. H. K. Kim, M. J. F. Digonnet, and G. S. Kino, "Air-core photonic-bandgap fiber-optic gyroscope," J. Lightwave Technol. **24**(8), 3169–3174 (2006).
5. N. Jay, "20 years of KVH fiber optic gyro technology," in *Fiber Optic Sensors and Applications XIII,* E. Udd, G. Pickrell, H. H. Du, eds., Proc. SPIE **9852** (2016).
6. J. Sawyer, P. B. Ruffin, and C. C. Sung, "Investigation of the effects of temporal thermal gradients in fiber optic gyroscope sensing coils," Opt. Eng. **36**(1), 29–34 (1997).
7. R. A. Bergh, L. Arnesen, and C. Herdman, "Fiber optic gyro development at Fibernetics," in *Fiber Optic Sensors and Applications XIII*, Proc. SPIE **9852** (2016).
8. T. Findakly and M. Bramson, "High-performance integrated-optical chip for a broad range of fiber-optic gyro applications," Opt. Lett. **15**(12), 673–675 (1990).
9. Y. Korkishko, V. Fedorov, S. Kostritskii, A. Alkaev, E. Paderin, E. Maslennikov, V. Kritzak, and D. Apraksin, "Integrated optical chip for fiber optical gyroscope fabricated by high temperature proton exchange," in *The 5th Pacific Rim Conference on Lasers and Electro-Optics* (2000).
10. A. Rickman, "The commercialization of silicon photonics," Nat. Photonics **8**(8), 579–582 (2014).
11. X. Yi and X. Wen, "Y-Integrated optic chip (Y-IOC) applied in fiber optic gyro," in *Advanced Laser Technologies*, Ivan A. Shcherbakov, Kexin Xu, Qingyue Wang, Alexander V. Priezzhev, Vladimir I. Pustovoy, eds., Proc. SPIE **6344** (2006).
12. J. F. Bauters, M. J. R. Heck, D. John, D. Dai, M.-C. Tien, J. S. Barton, A. Leinse, R. G. Heideman, D. J. Blumenthal, and J. E. Bowers, "Ultra-low-loss high-aspect-ratio Si_3N_4 waveguides," Opt. Express **19**(4), 3163–3174 (2011).
13. S. Srinivasan, R. Moreira, D. Blumenthal, and J. E. Bowers, "Design of integrated hybrid silicon waveguide optical gyroscope," Opt. Express **22**(21), 24988–24993 (2014).
14. T. Huffman, M. Davenport, M. Belt, J. Bowers, and D. Blumenthal, "Ultra-low loss large area waveguide coils for integrated optical gyroscopes," IEEE Photonics Technol. Lett. **99**, 1 (2016).
15. D. Huang, S. Srinivasan, and J. E. Bowers, "Compact Tb doped fiber optic current sensor with high sensitivity," Opt. Express **23**(23), 29993–29999 (2015).
16. S. Srinivasan and J. E. Bowers, "Integrated high sensitivity hybrid Silicon magnetometer," IEEE Photonics Technol. Lett. **26**(13), 1321–1324 (2014).
17. T. Komljenovic, M. Davenport, J. Hulme, A. Y. Liu, C. T. Santis, A. Spott, S. Srinivasan, and J. E. Stanton, C. Zhang and J. E. Bowers, "Heterogeneous Silicon photonic integrated circuits," J. Lightwave Technol. **34**(1), 20–35 (2016).
18. M. Tran, S. Gundaravapu, M. Belt, T. Komljenovic, D. Blumenthal, and J. E. Bowers, "Frequency modulated laser based interferometric optical gyroscope," in *Conference on Lasers and Electro-Optics* (2016)
19. T. Komljenovic, M. A. Tran, M. Belt, S. Gundavarapu, D. J. Blumenthal, and J. E. Bowers, "Frequency modulated lasers for interferometric optical gyroscopes," Opt. Lett. **41**(8), 1773–1776 (2016).

#281934 https://doi.org/10.1364/OE.25.003826
Journal © 2017 Received 2 Dec 2016; revised 6 Jan 2017; accepted 6 Jan 2017; published 13 Feb 2017

Optics EXPRESS

20. J. M. Machkintosh and B. Culshaw, "Analysis and observation of coupling ratio dependence of Rayleigh backscattering noise in a fiber optic gyroscope," J. Lightwave Technol. **7**(9), 15575–15586 (1989).
21. Y. Zheng, D. K.-T. Ng, Y. Wei, W. Yadong, Y. Huang, and Y. Tu, "Electrically pumped heterogeneously integrated Si/III-V evanescent lasers with micro-loop mirror reflector," Appl. Phys. Lett. **99**(1), 011103 (2011).
22. M. Tran, T. Komljenovic, J. Hulme, M. Davenport, and J. Bowers, "A robust method for characterization of optical waveguides and couplers," IEEE Photonics Technol. Lett. **28**(14), 1517–1520 (2016).
23. H. Park, A. W. Fang, R. Jones, O. Cohen, O. Raday, M. N. Sysak, M. J. Paniccia, and J. E. Bowers, "A hybrid AlGaInAs-silicon evanescent waveguide photodetector," Opt. Express **15**(10), 6044–6052 (2007).
24. H. Ohe, H. Shimizu, and Y. Nakano, "InGaAlAs Multiple-Quantum-Well Optical Phase Modulators Based on Carrier Depletion," IEEE Photonics Technol. Lett. **19**(22), 1816–1818 (2007).
25. H.-W. Chen, Y.-H. Kuo, and J. E. Bowers, "A hybrid Silicon–AlGaInAs phase modulator," IEEE Photonics Technol. Lett. **20**(23), 1920–1922 (2008).
26. S. W. Lloyd, M. J. F. Digonnet, and S. Fan, "Modeling coherent backscattering errors in fiber optic gyroscopes for sources of arbitrary line width," J. Lightwave Technol. **31**(13), 2070–2078 (2013).
27. R. A. Bergh, H. C. Lefevre, and H. J. Shaw, "Compensation of the optical Kerr effect in fiber-optic gyroscopes," Opt. Lett. **7**(6), 282–284 (1982).
28. R. Adar, C. H. Henry, R. F. Kazarinov, R. C. Kistler, and G. R. Weber, "Adiabatic 3-dB couplers, filters, and multiplexers made with silica waveguides on silicon," J. Lightwave Technol. **10**(1), 46–50 (1992).
29. S. Kimmo, M. Kapulainen, M. Harjanne, and T. Aalto, "Adiabatic and multimode interference couplers on silicon-on-insulator," IEEE Photonics Technol. Lett. **18**(21), 2287–2289 (2006).
30. H. Yun, W. Shi, Y. Wang, L. Chrostowski, and N. A. F. Jaeger, "2x2 Adiabatic 3-dB Coupler on Silicon-on-Insulator Rib Waveguide," in *Photonics North*, P. Cheben, J. Schmid, C. Boudoux, L. R. Chen, A. Delâge, S. Janz, R. Kashyap, D. J. Lockwood, H-P. Loock, Z. Mi, eds., Proc. SPIE **8915** (2013).
31. D. Taillaert, W. Bogaerts, P. Bienstman, T. Krauss, P. V. Daele, I. Moerman, S. Verstuyft, K. D. Mesel, and R. Baets, "An Out-of-Plane Grating Coupler for Efficient Butt-Coupling Between Compact Planar Waveguides and Single-Mode Fibers," IEEE J. Quantum Electron. **38**(7), 949–955 (2002).
32. T. Shoji, T. Tsuchizawa, T. Watanabe, K. Yamada, and H. Morita, "Low loss mode size converter from 0.3pm square Si wire waveguides to singlemode fibres," Electron. Lett. **38**(25), 1669–1670 (2002).
33. A. W. Fang, H. Park, O. Cohen, R. Jones, M. J. Paniccia, and J. E. Bowers, "Electrically pumped hybrid AlGaInAs-silicon evanescent laser," Opt. Express **14**(20), 9203–9210 (2006).
34. E. Kiesel, "Impact of modulation induced signal instabilities on fiber gyro performance," in *Fiber Optic and Laser Sensors V*, R. P. DePaula; E. Udd, eds., Proc. SPIE **838** (1987).
35. Y. Shen, M. Tran, S. Srinivasan, J. Hulme, J. Peters, M. Belt, S. Gundavarapu, Y. Li, D. Blumenthal, and J. Bowers, "Frequency modulated laser optical gyroscope," in *IEEE Photonics Conference* (2015).
36. H. Ma, J. Zhang, L. Wang, Y. Lu, D. Ying, and Z. Jin, "Resonant micro-optic gyro using a short and high-finesse fiber ring resonator," Opt. Lett. **40**(24), 5862–5865 (2015).
37. C. Ciminelli, F. Dell'Olio, M. N. Armenise, F. M. Soares, and W. Passenberg, "High performance InP ring resonator for new generation monolithically integrated optical gyroscopes," Opt. Express **21**(1), 556–564 (2013).

1. Introductions

The interferometric fiber optic gyroscope (IFOG) was proposed in 1968 [1] and has been developed for decades until the technology and understanding of performance limitations has reached sufficient levels for IFOGs to be commercially used. Today IFOG is a mature technology that delivers high sensitivity, high stability and reliability. A modern IFOG comprises of three main components: a passive sensing coil, a set of active optical components and read-out electronics [2]. There has been tremendous development on perfecting the passive sensing parts with the invention of new types of fibers, *e.g.* hollow-core fibers with significantly reduced non-linear and thermal effects [3,4], high polarization extinction ratio fibers to reduce the polarization coupled drift [5]. In addition, more complex fiber winding techniques such as quadrupole or octupole symmetry were introduced to cancel out non-reciprocal noise and drift due to thermal gradients and vibration [6]. Further improvement includes using thinner claddings (80 um) or even multicore fibers to significantly reduce the size of the sensing coil, but keep high sensitivity due to long fiber lengths [7].

However, the optical components that generate, modulate and detect the optical signal to drive the optical gyroscopes have not evolved comparably. Most modern IFOGs use discrete optical components and these components are normally packaged with fiber pigtails to form the Sagnac reciprocal interferometer optical circuit [2]. Even though using discrete parts offers the freedom of choosing the best performing components, it can result in a number of parasitic reflections, increased insertion losses at connection points, and environmentally

Optics EXPRESS

sensitive polarization misalignments that degrade the performance. Although it is possible to minimize these effects, for example with mode and polarization filters, careful and costly packaging efforts are required. In addition, the use of discrete components also results in larger size and weight.

The idea of using integrated optics in IFOGs was introduced early in literature [8–10], but the research results have been limited. The most widely-used implementation of integrated optics in gyroscope technology is the so-called integrated optical chip (IOC) that integrates a Y-junction and phase modulator using a $LiNbO_3$ waveguide [11].

In this work, we present the first fully integrated optical driver (IOD) chip that comprises all optical active components and passive components needed for optical gyroscopes except the sensing coil. The chip can be interfaced with a delay sensing coil, such as optic fiber or an ultra-low loss waveguide [12–14], to form a working interferometric optical gyroscope. It can also be readily used for current sensing and magnetometer if the delay coil is replaced by a Tb-doped fiber [15] or hybrid Ce:YiG-Si_3N_4 waveguide [16]. The chip is designed and fabricated using the heterogeneous III-V/Si photonics integration technology [17].

The paper is organized as follows. In Section 2, we first show the circuit layout of the IOD chip with target specifications. Section 3 follows with details of each component's design. Details on the fabrication process are explained in Section 4. Section 5 presents the characterization of each component and the rotation measurement of the IFOG using the fabricated IOD. The paper concludes in Section 6 with a summary and discussion of outlook.

2. Design of the integrated optical driver for fiber optic gyroscopes

The schematic layout of the IOD chip is illustrated in Fig. 1(a). The light source is a multi-mode Fabry-Perot laser, that can be frequency modulated to reduce its coherence length and improve the gyroscope performance towards that of amplified spontaneous emission (ASE) sources [18,19]. Utilization of a laser significantly reduces the power consumption over for example a super luminescent light emitting diode (SLED) as above threshold most of the current is converted to photons. Three photodiodes are used to detect the Sagnac signal and provide a monitor for the laser output. Corrections to the read-out of the gyroscope or stabilization of the laser power by an electrical feedback loop are straightforward to implement since the control and feedback signals are available in the IOD. The phase modulators are laid out in a push-pull configuration to reduce the half-wave voltage. The two power splitters should ideally have 50% splitting ratio to reduce the backscattering noise and maximize the intensity of the Sagnac signal [20] [13]. We address our coupler design in detail in later sections. The two output waveguides are inversely tapered for mode matching with optical fibers. We intentionally bring the two output waveguides to the opposite sides of the chip; it is expected that having uneven distances from the 3-dB splitters to the waveguide facets (ideally the difference between these distances should be larger than coherence length of the light source [2] [13]) would help reduce the coherent back-reflection noise induced by the reflections at the chip-fiber interfaces. All the active components (*i.e.* lasers, photodiodes and phase modulators) are designed on the III-V/Si heterogeneous integration platform, and we provide details in later sections. The silicon-on-insulator (SOI) wafer used has a 500 nm thick device layer on top of 1 μm buried oxide. Schematic of the cross section of heterogeneous integrated devices is shown in Fig. 1(b).

When operating in a gyroscope system, the phase modulator will be modulated at the proper frequency of the gyroscope, which is strictly related to the length of the sensing coil by equation $f_p = \frac{\pi c}{n_{eff} L}$ where c is the speed of light in vacuum, n_{eff} is the effective index of the propagation mode and L is the length of the coil. Depending on the performance requirements and applications, the length of the sensing coil may vary from tens of meters to several kilometers, resulting in the proper frequency range from hundreds of kHz to hundreds of

Optics EXPRESS

MHz. Different modulation signals (sinusoidal, squared, triangle wave, etc.) can be used. To cover all potential fiber lengths with sufficient margin, we have designed both the modulators and the detectors to have bandwidths greater than 1 GHz.

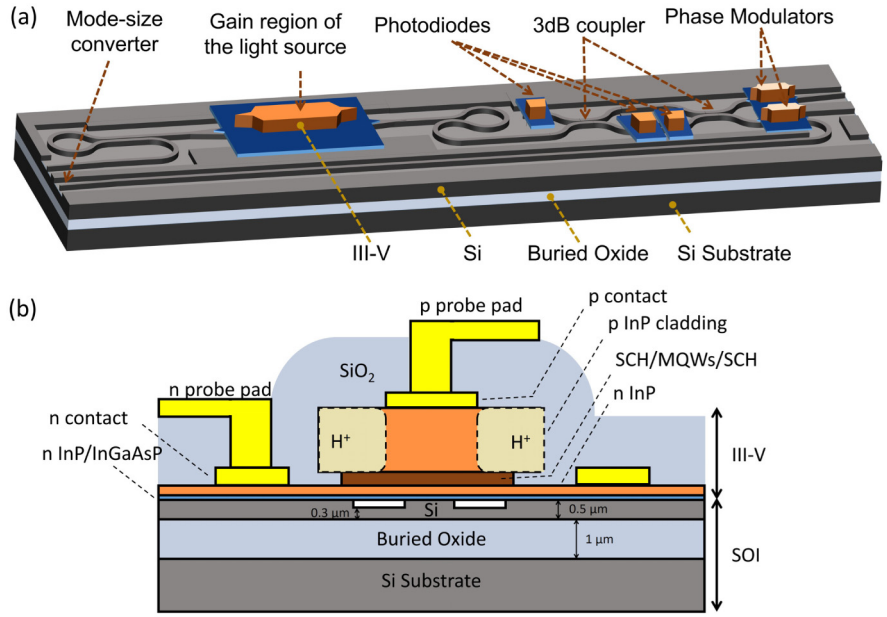

Fig. 1. (a) 3D schematic (not to scale) of the integrated optical driver (IOD) for fiber optic gyroscopes. (b) Cross section of III-V/Si heterogeneously integrated active components (lasers, photodiodes and modulator).

3. Designs of components

3.1. Light source

A multi-mode Fabry-Perot laser is utilized in the IOD chip. The schematic of the laser design is shown in Fig. 2. The III-V layer stack used as gain element for the laser has three strained InAlGaAs quantum wells (QWs) sandwiched between two separate confinement hetero-structure (SCH) layers, as shown in Table 1. The Si rib waveguide is 500 nm tall and 750 nm wide, with 200 nm etched depth.

Table 1. Epitaxial III-V Layer Structure Used for the Lasers and Photodiodes

Layer Name	Layer Composition	Thickness (µm)	Doping level
P-contact	P-In0.53Ga0.47As	0.1	1.50E+19
Smoothing	P-1.5Q $In_{0.586}Ga_{0.414}As_{0.888}P_{0.112}$	0.025	3.00E+18
Smoothing	P-1.3Q $In_{0.729}Ga_{0.271}As_{0.587}P_{0.413}$	0.025	3.00E+18
P-cladding	P-InP	1	1.50E+18
P-cladding	P-InP	0.2	8.00E+17
P-cladding	P-InP	0.25	5.00E+17
SCH	N-$In_{0.53}Al_{0.183}Ga_{0.287}As$	0.125	1.00E+17
MQW	U-3 x $In_{0.6758}Al_{0.06}Ga_{0.2642}As$ Well (+1% CS)	3 x 0.006	
	U-4 x $In_{0.4411}Al_{0.085}Ga_{0.4739}As$ Barrier (-0.6% TS)	4 x 0.009	
SCH	N-$In_{0.53}Al_{0.183}Ga_{0.287}As$	0.125	1.00E+17
N-Contact	N-InP	0.11	2.00E+18
Superlattice	2 x N-$In_{0.85}Ga_{0.15}As_{0.327}P_{0.673}$	0.0075	1.00E+18
	2 x N-InP	0.0075	
Bonding layer	N-InP	0.01	1.00E+18

The laser cavity mirrors are formed by two loop mirrors that are realized in silicon, similar to [21]. We chose loop mirrors as they can be formed anywhere on chip (no need for facets)

Optics EXPRESS

and the reflectivity can be chosen arbitrarily based on the coupling ratio of the coupler used. When the insertion loss of the coupler is negligible, the relationship between the reflectivity ($\mathcal{R}$) of the loop mirror and the coupling ratio (k) of the 2 × 2 coupler is given by equation $\mathcal{R} = 4k(1-k)$ and plotted in Fig. 3 (the derivation can be achieved using transfer matrix method, similar to MZI modeling carried out in [22]). For the gyroscope IOD's Fabry-Perot laser, the mirror on one side is designed to be nearly total reflective while the other one is 70% reflective so that all the generated photons are guided towards the sensing part. The high reflective mirror on the left hand side makes use of a 3-dB adiabatic coupler to allow a high reflectivity over a broad optical bandwidth, whose details will be explained in Section 3.4. The lower reflective mirror on the right hand side uses a directional coupler with 23% designed coupling ratio.

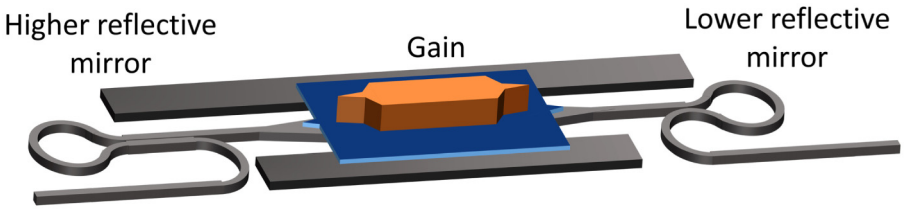

Fig. 2. Schematic of the Fabry-Perot laser with the gain region on III-V layer and the integrated loop mirrors on Si. The two mirrors' reflectivities are designed to be 100% on one side (left) and 70% on the other side (right) to direct most of output power towards the rest of the PIC (on the right hand side of the laser).

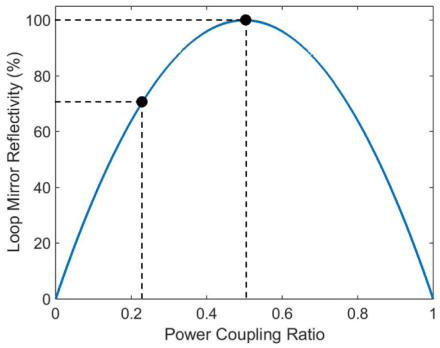

Fig. 3. Relation between loop mirror reflectivity versus coupling ratio of the 2 × 2 coupler when its insertion loss is negligible, which is applicable for directional couplers. Two highlighted points are chosen for the FP laser loop mirrors.

3.2 Photodiode

The photodiode used the identical three quantum well III-V stack as the gain described in section 3.1. The device design was similar to the one demonstrated by Park et al. [23] in which the III-V region was tilted to reduce the reflection at the waveguide transition (see Fig. 4). Along the hybrid region, the Si waveguide width was gradually tapered from 3 μm to 600 nm to push the mode vertically and increase the confinement factor in the quantum well region, thus achieving higher absorption and responsivity.

Optics EXPRESS

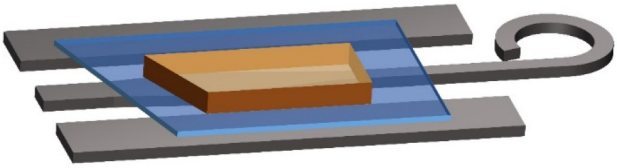

Fig. 4. Schematic of the photodiode. The III-V layers are drawn transparent to show the change in the width of the underneath Si waveguide.

3.3 Phase modulator

For phase modulation, we utilized the carrier depletion effect in multiple quantum wells of AlGaInAs to realize phase modulators with broad optical bandwidth, low insertion loss and low power consumption [24]. The III-V stack for the phase modulator was modified from the design reported by Hui-wen et al. [25] and is shown in Table 2. The modification was necessary to match the thicknesses of the III-V layers for lasers and photodiodes so that a single etching process could be done simultaneously for all different III-V stacks. In addition, the phase modulators were laid out in a push-pull configuration to benefit in lowering the backscattering noise as discussed in [26]. The schematic of the push-pull modulators with the metal-probe layout on the top is illustrated in Fig. 5(a) and the circuit driving the push-pull operation is shown in Fig. 5(b).

Table 2. Epitaxial III-V Layer Structure Used for the Phase Modulators

Layer Name	Layer Composition	Thickness (μm)	Doping level
P-contact	P-$In_{0.53}Ga_{0.47}As$	0.1	1.50E + 19
Smoothing	P-1.5Q $In_{0.586}Ga_{0.414}As_{0.888}P_{0.112}$	0.025	3.00E + 18
Smoothing	P-1.3Q $In_{0.729}Ga_{0.271}As_{0.587}P_{0.413}$	0.025	3.00E + 18
P-cladding	P-InP	1	1.50E + 18
P-cladding	P-InP	0.25	8.00E + 17
P-cladding	P-InP	0.25	5.00E + 17
SCH	N-$In_{0.5284}Al_{0.193}Ga_{0.2786}As$	0.1	1.00E + 17
MQW	U-15 x $In_{0.574}Al_{0.111}Ga_{0.315}As$	15 x 0.008	1.00E + 17
	U-16 x $In_{0.468}Al_{0.217}Ga_{0.315}As$	16 x 0.005	1.00E + 17
SCH	N-$In_{0.5284}Al_{0.193}Ga_{0.2786}As$	0.05	3.00E + 18
N-Contact	N-InP	0.11	3.00E + 18
Superlattice	2 x N-$In_{0.85}Ga_{0.15}As_{0.327}P_{0.673}$	0.0075	1.00E + 18
	2 x N-InP	0.0075	
Bonding layer	N-InP	0.01	1.00E + 18

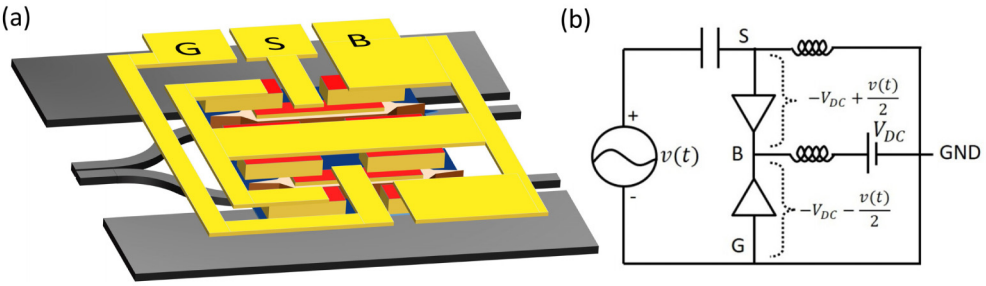

Fig. 5. (a) Schematic of push-pull modulators for the IOD. (b) The circuit diagram for the push-pull modulation operation.

3.4 Three-dB coupler

Having an exact 50% coupler over the operational wavelength range is crucial for the gyroscope IOD chip. The non-equal splitting of the coupler can cause the increase in backscattering induced noise [20] [13] and Kerr effect [27], both of which degrade the performance. In integrated photonics, multimode interference (MMI) couplers and directional

Optics EXPRESS

couplers are often preferred for their compact size. However, MMIs in general have higher insertion losses and reflections. As parasitic reflections must be strictly minimized in the gyroscope, the MMI design is not preferred. Directional couplers, despite being low loss and low reflection, are highly sensitive to fabrication errors and are highly dependent on wavelength. For this reasons we used adiabatic 3-dB couplers/splitters [28–30] that are inherently wavelength insensitive, more fabrication tolerant and provide equal splitting. These benefits, however, come along with a trade-off in requiring a longer structure.

Our design of an adiabatic 3-dB 2 × 2 coupler is illustrated in Fig. 6(a). The coupler comprises three sections: the first section (300 µm long) where the two ridge waveguides with different widths (600 nm and 800 nm wide) slowly come close to each other using S-bends, the coupling section (400 µm long) where the two asymmetric waveguides are linearly tapered to 700 nm wide waveguides, and the third section (300 µm long) where each 700 nm wide waveguide is guided to one of the output waveguides by two other S-bends. We used FIMMPROP to simulate the propagation of modes through the structure. Figure 6(a) also shows, as an example, how the mode propagates and splits through the coupler when light is input to the 800 nm wide waveguide. The input mode first excites the fundamental (even) mode of the coupler modes, then this even mode transmits adiabatically to the even mode of the symmetric 700 nm wide waveguides at the end of the coupling section; after that, the power then splits equally to the two output waveguides. The simulation result (Fig. 6(b)) shows 50 ± 3% splitting ratio of the adiabatic coupler over C-band.

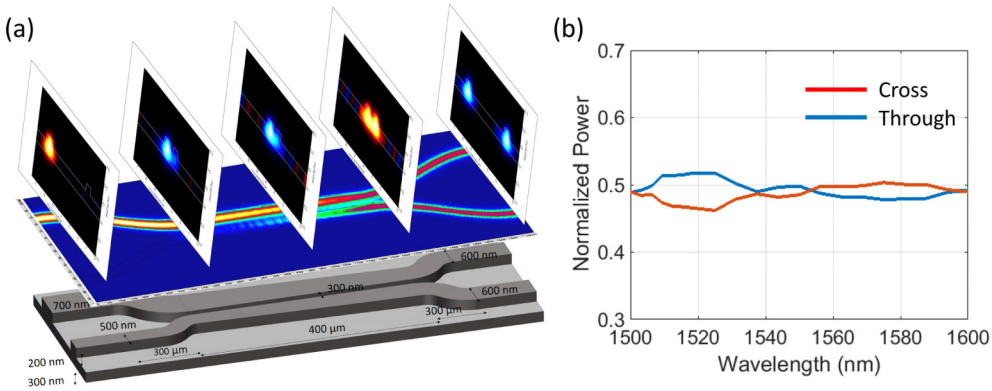

Fig. 6. (a) Schematic of the 3-dB adiabatic coupler. The simulated mode evolution along the coupler is shown to illustrate the working principle. (b) Simulated wavelength dependence of the coupler

3.5 Mode size converter

Due to the large mismatch in the mode field size between Si waveguide and optical fiber, it is necessary to have a mode size converter at the interface. The two main approaches that are widely used include vertical grating couplers [31] and edged couplers [32]. Since grating couplers in general have a limited optical bandwidth and an inherent back reflection, edged coupling is chosen for use in our IOD chip. The schematic design of the mode size converter transitioning from 500 nm thick Si waveguide to optical fiber is shown in Fig. 7(a). The converter comprises two parts: a bi-level taper and an inversed taper. Through the bi-level taper, the optical mode from 500 nm x 600 nm rib Si waveguide is squished to the mode in thinner 300 nm x 600 nm Si waveguide. The waveguide is then tapered to 300 nm x 175 nm waveguide. Since the Si core is now too small, the optical mode is no longer well confined in Si but expands to the oxide cladding, largely increases the mode field area and lower the mode mismatch with optical fibers. The waveguide is also angled to 7° respective to the polished facet to decrease back reflection.

Optics EXPRESS

The bi-level taper was simulated with FIMMPROP and the averaged transmission loss over C-band was estimated to be −0.6 dB. In addition, the coupling efficiency from the Si inversed taper to a 2.5 μm spot-size fiber was done with FDTD Lumerical and the average coupling loss over C-band is about −2.05 dB, as shown in Fig. 7(b). In total, the mode converter is expected to have −2.7 dB coupling loss over C-band. All simulations only considered TE mode.

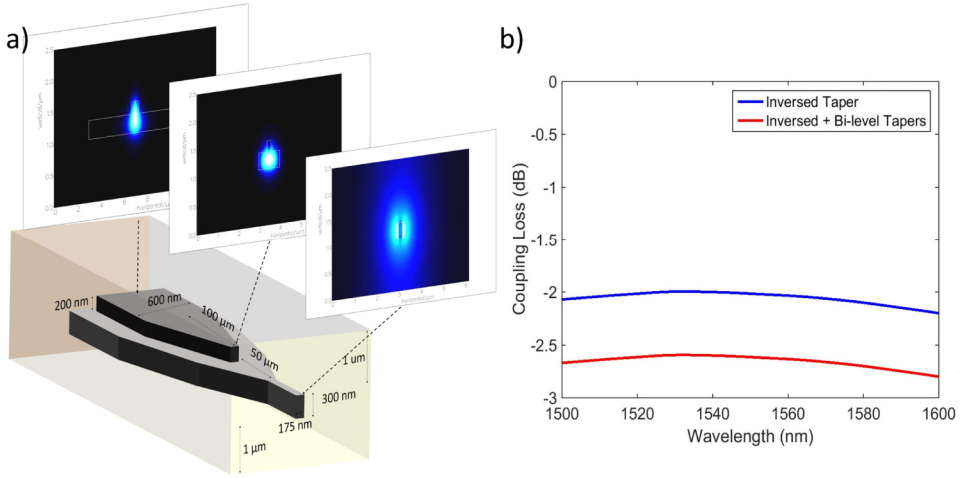

Fig. 7. (a) Schematic of the bi-level taper and the inversed taper for waveguide-fiber. The mode evolution along the coupler is shown to illustrate the working principle. (b) Blue curve: FDTD simulated coupling loss from 300 nm x 175 nm Si waveguide to 2.5 μm spot-size lensed fiber. Red curve: Total coupling loss including the bi-level taper. The waveguide was angled to 7° and the lensed fiber approach angle was 8° respective to the chip facet.

4. Fabrication

The fabrication of the heterogeneous integrated chip started with Si waveguide etching on an SOI substrate that has 500 nm thick Si on top of a 1 μm thick buried oxide layer. Rib waveguides were patterned on 248 nm DUV lithography and etched 200 nm with the SF_6/C_4F_8 plasma based deep reactive-ion etching (RIE). The second step of lithography and etching were followed to deeply etch strip waveguides and vertical channels for outgassing. Good alignment between these two lithography steps is important to achieve the desired bi-level taper structure for the waveguide-fiber couplers.

Two III-V epitaxial structures with details shown in Table 1 and 2 were grown on InP substrates and cleaved into pieces. These pieces were then bonded to the top silicon using low temperature hydrophilic bonding process [23] [33] to form active regions for the active components. The III-V substrates were then removed by mechanical polishing and chemical wet etching before the p-mesas were etched down into the MQWs region by $CH_4/H_2/Ar$ based plasma RIE. The separate confined hetero-structures (SCHs) and quantum wells were subsequently wet etched to n-type layers. Pd/Ge/Pd/Au/Ti alloy contacts were lifted-off to form n-metal layers. The III-V mesa on regions without active components was etched away by dry and wet etch, exposing passive Si waveguides and structures. Oxide coverage deposition was followed to protect the waveguides and to form electrical isolation between n-type layers and p-metal pads. Vias were opened by dry etch to allow for p-metal deposition. After proton implantation on two sides of the p-type mesas, Ti/Au stacks for probe pads were deposited. The fabrication was completed with dicing and Si facet polishing.

SEM images of the components on the IOD chip along the fabrication process are shown in Fig. 8. We had identical test structures for each component fabricated in the same process to allow for individual characterization.

Optics EXPRESS

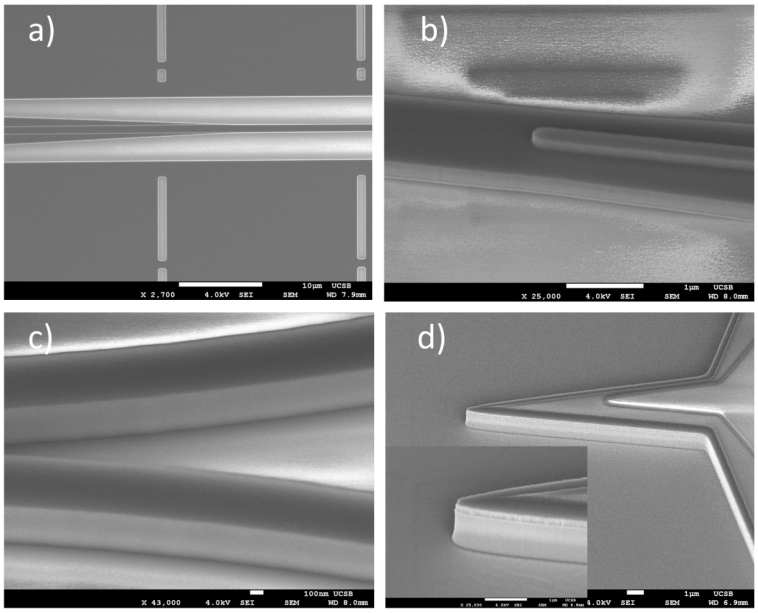

Fig. 8. SEM images of (a) Top view of the deep-shallow transition showing good lithography alignment for deep and shallow etch waveguides. (b) Tilted view of the bi-level taper. (c) Two adjacent waveguides with very smooth sidewalls. (d) Tilted view of the p-doped InP mesa after $CH_4/H_2/Ar$ based plasma RIE etch.

5. Results

A microscopic image of a completed IOD chip is shown in Fig. 9 with break-downs of each components. The chip is 9 mm x 0.5 mm in size. A bar that comprises 12 individual IODs is put next to a US quarter dollar for comparison.

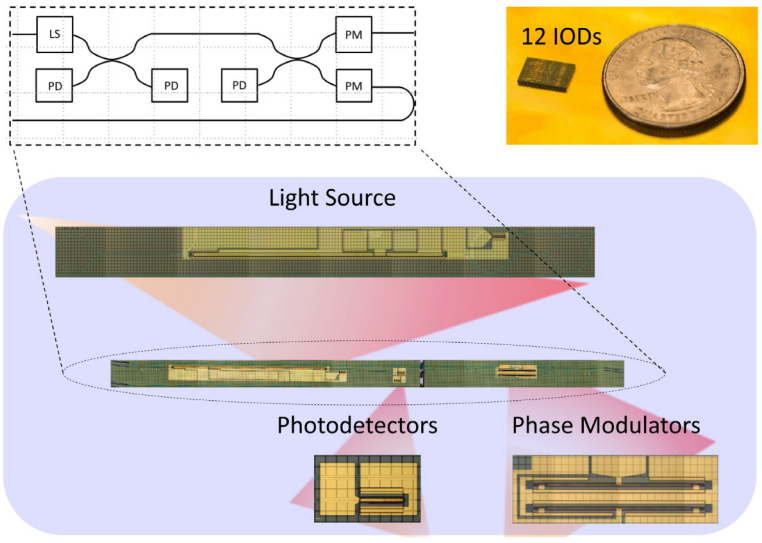

Fig. 9. Photograph of a fabricated IOD chip with close-ups of its components. LS: Light Source, PD: Photodiode, PM: Phase Modulator. A set of 12 devices next to a US quarter coin for size comparison.

Optics EXPRESS

5.1 Individual components

5.1.1 Fabry-Perot lasers

The current-output power curve of the Fabry-Perot laser at room temperature is shown in Fig. 10(a). The threshold current is about 40 mA. The laser's optical spectrum when operating at well above threshold (150 mA) is shown in Fig. 10(b). A multi-mode lasing across the 1578 – 1595 nm wavelength range was achieved with mode spacing of 0.07 nm corresponding to a cavity length of 4.5 mm formed by the two integrated loop mirrors.

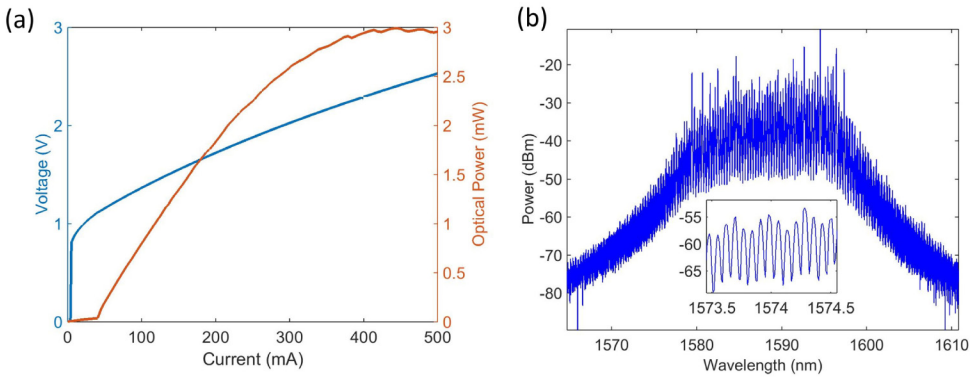

Fig. 10. (a) LIV curve of the laser. (b) Optical spectrum of the fabricated FP laser. The inset shows the mode spacing that corresponds to the laser cavity length.

5.1.2 Photodiodes

The dark-current is 4 nA at −3 V and goes up to 15 nA at −6 V bias, as shown in Fig. 11(a). The frequency response at wavelength of 1550 nm and −6 V reversed bias was measured using the Agilent N4373A Lightwave Component Analyzer (LCA) measurement setup and is shown in Fig. 11(b). The 3-dB bandwidth is larger than 6 GHz up to 1 mA photocurrent, with a responsivity of about 0.7 A/W.

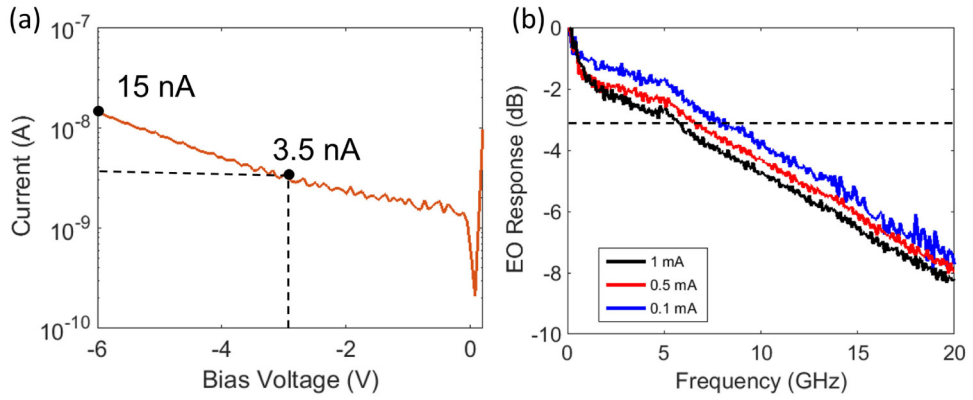

Fig. 11. (a) Photodiode voltage-current curve at reversed bias. (b) Frequency response at different levels of photocurrent.

5.1.3 Phase modulators

To measure the insertion loss of the modulators, the transmission spectrum through a stand-alone phase modulator was measured and compared with that of a reference single straight waveguide. At a reverse bias smaller than 3 V, the insertion loss is less than 1 dB over C-band. The phase modulator was also placed in a Mach-Zehnder Interferometer (MZI) test

Optics EXPRESS

structures to form an MZI modulator for half-wave voltage and frequency response characterization. The optical power (wavelength 1550 nm) from the output waveguide of the MZI modulator was measured while DC reverse bias voltage was swept from 0 to 6 V as shown in Fig. 12(a). The half-wave voltage for 500 μm long structure is 8.4 V. The high speed performance was measured at varying reverse bias voltages using an HP 8703A LCA setup. The modulator exhibited a 3 dB bandwidth of about 2 GHz at −2 V bias as shown in Fig. 12(b).

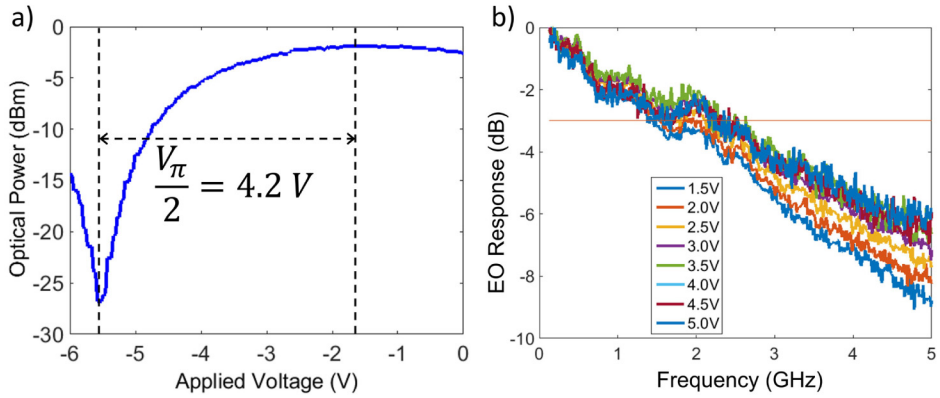

Fig. 12. (a) MZI modulator's half-wave voltage measurement at DC bias. (b) Its frequency response at varying reversed-biases showing 3-dB bandwidth of 2 GHz.

5.1.4 Three-dB coupler

The 2 × 2 adiabatic 3-dB coupler was characterized by using a rigorous method reported in [22]. The measurement setup is shown in Fig. 13(a) with a high-precision tunable laser source, high precision power sensor, a polarization controller and a polarizer and polarization maintaining (PM) fibers. The lensed fiber holder rotator was adjusted to launch TE mode (polarization extinction ratio TE/TM > 25 dB) prior to testing.

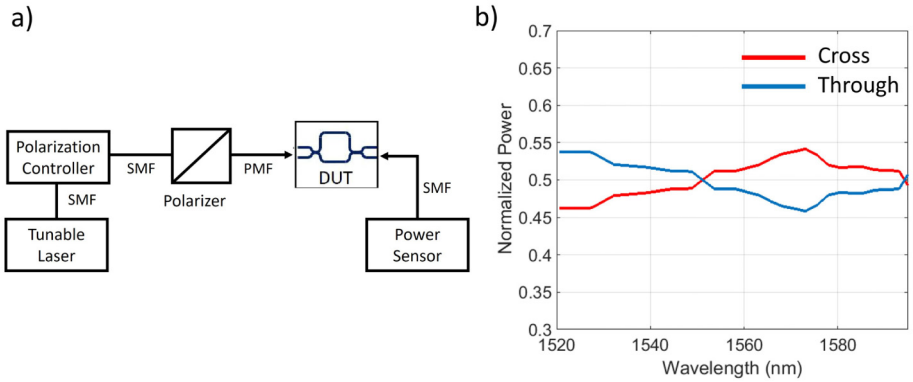

Fig. 13. (a) Measurement setup for testing passive components. (b) Normalized splitting ratios of the fabricated adiabatic 3-dB splitter, extracted using the UMZI spectra analysis.

The splitting ratios versus wavelength plot of the coupler are shown in Fig. 13(b). The splitter exhibited a flat wavelength response over the C-band. The normalized power splitting ratio over 75 nm wavelength range (1520 – 1595) was within 50 ± 4.2%.

Based on Fig. 3, given loss-less assumption, the loop mirror using adiabatic coupler should have around 99% reflectivity over the above wavelength range. The Si waveguide propagation loss was measured to be about 1.5 dB/cm; thus it makes up to about 0.2 dB total

Optics EXPRESS

loss for the whole loop mirror structure. Combining both, we estimate the reflectivity of the adiabatic coupler based loop mirror to be around 94% over the C-band.

5.1.5 Mode size converter

The coupling loss of the converter was characterized using the setup shown in Fig. 13(a). PM lensed fibers with the mode diameter of ~2.5 μm were used to couple the Si waveguide with mode size converters. Transmission power through a Si straight waveguide with two mode converters at two ends was recorded while laser wavelength was swept over 1525 – 1575 nm. The same measurement was also taken for transmission from fiber to fiber as a reference. The coupling efficiency was then extracted, taking into account the extra 0.2 dB propagation loss of the 0.2 mm Si straight waveguide, as shown in Fig. 14. The averaged coupling loss is determined to be −3 dB. The 0.3 dB discrepancy between measurement and simulation (Section 3.5) can be attributed to the propagation loss along the mode converter structure.

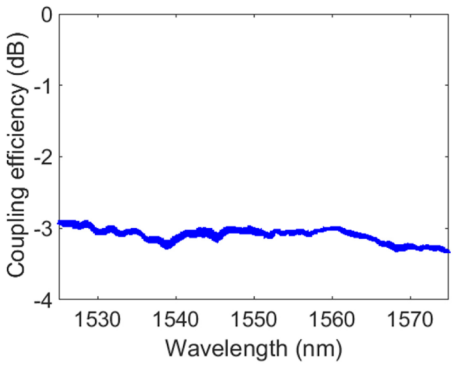

Fig. 14. Coupling efficiency between TE mode of the Si waveguide and 2.5 μm mode diameter lensed fiber.

5.2 Rotation sensing measurement and discussion

To test the functionality of fabricated IOD chip, we formed an open-loop interferometric optical gyroscope by connecting the chip to a 180 m long polarization maintaining (PM) fiber coil with bench-top read-out electronics illustrated in Fig. 15(a). The fibers were aligned to the mode size converters of the IOD by using two 3-axis stages and electrical contacts to the chip were made by using RF probes (shown in Fig. 15(b)). The chip was kept at room temperature by a thermoelectric cooler underneath the stage. The entire alignment setup was placed on an optical bench while the fiber coil was put on a separate rotation table; hence, it is possible to apply the rotation only to the sensing coil without disturbing the optical and electrical alignments on the chip. A 20 dB RF amplifier was used to boost the interference signal at the first photodiode on the IOD. The signal was analyzed with an electrical spectrum analyzer (ESA).

Optics EXPRESS

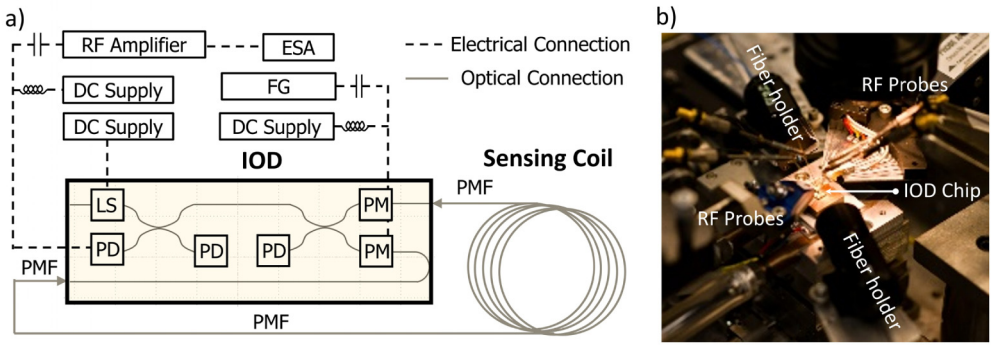

Fig. 15. (a) Schematic of the interferometric optical gyroscope driven by the IOD chip. The PM fiber coil is 180 m long with a diameter of 20 cm. LS: Light Source, PD: Photodiode, PM: Phase Modulator, PMF: Polarization Maintaining Fiber, ESA: Electrical Spectrum Analyzer, FG: Function Generator. (b) Photograph of the electrical and optical alignment onto the IOD chip.

In operation of the IOD, the DC current to the laser was set at 400 mA, well above the threshold current and near the maximum output power point. The phase modulators and photodiodes were operated in reverse bias regime. The total photo-current received at the detection photodiode was 8 μA, corresponding to 1.14 μW optical power. A sinusoidal wave was applied to the phase modulator at the proper frequency of $f_p = 560\,\text{kHz}$ which is governed by the length of the fiber coil [2]. The modulation amplitude on the phase modulator was set to 250 mV, corresponding to modulation depth of about $\phi_b = 0.1$ rad. The rotation induced Sagnac phase shift is $\Delta\phi_R = \frac{8\pi LD}{\lambda c}\frac{\pi}{180}\Omega_R$ where $L = 180\,\text{m}$ is the length, $D = 0.2\,\text{m}$ is the diameter of the coil, $\lambda = 1.57\,\mu\text{m}$ is the mean-wavelength of the multimode laser and Ω_R (°/s) is the rotation rate. Due to the sinusoidal modulation of the phase modulator, the gyroscope output voltage is given by

$$V(\Omega_R) = I_0 R_{ESA} G J_1(\phi_b) \sin\Delta\phi_R \qquad (1)$$

where $I_0 = 8\,\mu\text{A}$ is the detected DC photocurrent, $R_{ESA} = 50\,\Omega$ is the resistance of the ESA, $G = 10$ is the amplification of the RF amplifier and $J_1(\phi_b = 0.1)$ is the Bessel function of the first order at the phase modulation depth. Using the small angle approximation for sin function, we can estimate $V(\Omega_R) \approx 6.70\times10^{-6}\Omega_R$, in other words, the scale factor of the gyroscope is expected to be $6.70\,\mu\text{V/(°/s)}$.

We carried out the gyroscope measurement by sweeping the rotation rates in clockwise (CW) and counter-clockwise (CCW) directions alternately and recorded the voltage at the modulation frequency on the ESA. The output signal voltage versus the rotation rate is plotted in Fig. 16(a). It shows that the gyroscope output was linearly proportional to the applied rotation rate with a scale factor of $6.28\,\mu\text{V/(°/s)}$. This is in good agreement with the above calculation; the measured value is slightly smaller possibly due to some signal losses along the RF connections in the setup.

Optics EXPRESS

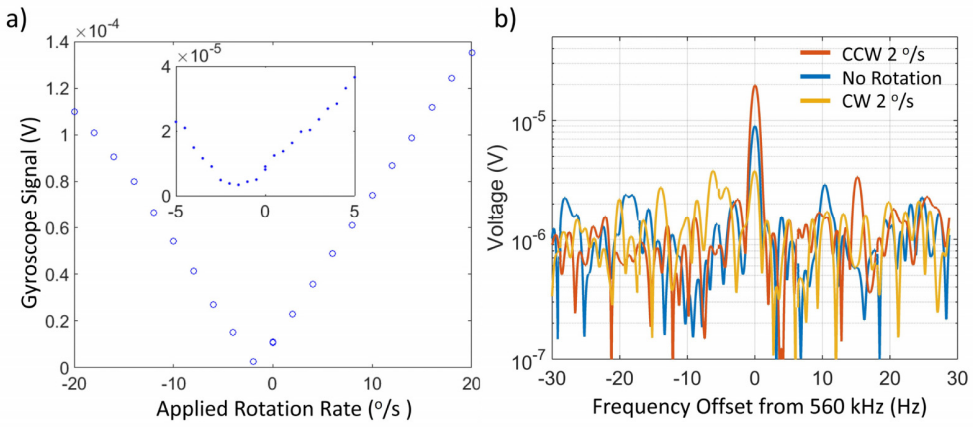

Fig. 16. (a) IOD driven gyroscope's signal versus the rotation rate. Inset shows a zoom-in of small range of the rotation rate. (b) The spectra on the ESA of CW and CCW 2 °/s and zero-rotation. The plot is centered at the 560 kHz modulation frequency with the resolution width of 1 Hz.

We can observe that there is an offset of roughly 2 °/s in the rotation measurement. As revealed in the ESA spectra shown in Fig. 16(b), when no rotation was applied, there still appeared at the modulation frequency a peak of 8.5 μV of an "offset signal" that is not caused by Sagnac phase shift. The possible causes for this offset could be electromagnetic interference (EMI) between components on the integrated circuit chip or phase error caused by residual amplitude modulation of the phase modulator [34]. Earth rotation and magnetic field induced nonreciprocal phase shift [15] could also contribute a fraction to the offset. Nonetheless, the offset caused by these effects can be calibrated out to correct the gyroscope's read-outs in practice.

Currently, the minimum measurable rotation rate was limited to about 3.39 μV or equivalent 0.53 °/s rotation rate (Fig. 16(a) inset). It is mainly limited by a low signal to noise ratio (S/N), as can be seen on the spectrum of CW 2 °/s rotation in Fig. 16(b). Larger S/N is necessary for improving the gyroscope sensitivity. To enhance the signal amplitude, we can increase the scale factor in Eq. (1) by choosing the optimal modulation depth for the phase modulator to maximize $J_1(\phi_b)$ and by having larger gain G in the RF amplifier. To suppress the noise floor, it has been shown in [35] that frequency modulating the laser is a useful technique. Combining these methods, we can expect to obtain at least two order of magnitude improvement on the sensitivity of the gyroscope.

For more in-depth understanding of all the existing noise processes in the IOD driven gyroscope system, time dependent measurements (similar to those in [19]) are required. Due to the drift in coupling between the optical fibers and the waveguides on chip, we were unable to make stable extended measurements needed for the Allan deviation. For proper characterization of the gyroscope's key parameters *e.g.* angle random walk and bias stability, permanent optical and electrical packaging of the device is needed. This is an ongoing work and we will report the results in a future publication.

6. Conclusion and outlook

We have presented the design, fabrication and characterization of an integrated optical driver (IOD) for interferometric optical gyroscopes. The IOD contains a Fabry-Perot multi-mode laser, photodiodes, phase modulators and adiabatic 3-dB splitters on a single chip within a 0.5 mm x 9 mm area. We have succeeded in demonstrating, for the first time, a working IFOG driven by a fully integrated chip.

Optics EXPRESS

In future work, more characterizations on packaged device are needed in order to complete the evaluation of the IOD-driven-gyroscope. Understanding the noise characteristics and limitations is beneficial for improvement in the next generation of IODs. In addition, demonstration of closed loop FOGs driven by the IOD to achieve high dynamic range and sensitivity is of great interest.

It is worth noting that the same IOD can be exploited in other sensing applications such as magnetometer and current sensor just by interrogation with special sensing waveguide and fibers [16]. Furthermore, with proper modifications in circuit design, IODs that are applicable for resonant optical gyroscopes, such as with an external fiber ring [36] or on-chip waveguide ring resonator [37], are also straight forward to achieve. Heterogeneous integration technology can cause the size, weight, cost and power consumption for optical gyroscopes and optical sensors in general to be greatly reduced while improving the shock and vibration robustness.

Funding

Defense Advanced Research Projects Agency (DARPA) (HR0011-14-C-0111).

Acknowledgments

The authors would like to thank Chao Xiang for help with simulation, Michael Davenport and Dr. Chong Zhang for III-V epitaxial designs, Dr. Jin-Wei Shi and Dr. Shangjian Zhang for high speed measurements, Tony Huang, Jon Peters, Sarat Gundaravapu, Taran Huffman, and Michael Belt for technical help, Dr. Robert Lutwak, Dr. Larry Coldren and Dr. Jon Schuller for fruitful discussions.

This research was developed with funding from the Defense Advanced Research Projects Agency (DARPA) within the Microsystems Technology Office Positioning, Navigation and Timing under Grant HR0011-14-C-0111. The views, opinions and/or findings expressed are those of the authors and should not be interpreted as representing the official views or policies of the Department of Defense or the U.S. Government.